T. Dang, Z. Liu, M. Morandini, L. Ma, P. Masarati
Bifurcation and Chaos Analysis of a Supersonic Slipper-Track System
Journal of Computational and Nonlinear Dynamics, Vol. 19, N. 8, 081003 (14 pages), 2024
(published online 30/05/2024)
doi:10.1115/1.4065629

Bifurcation and chaos analysis of a supersonic slipper-track system

Tianjiao Dang[1]
The first affiliation:
State Key Laboratory for Strength and Vibration of Mechanical Structures, Xi'an Jiaotong University
No. 28, Xianning West Road, 710049, Xi'an, Shaanxi, P.R. China
The second affiliation:
Department of Aerospace Science and Technology, Politecnico di Milano
Via La Masa 34, 20156 Milano, Italy
tianjiao.dang@polimi.it

Zhen Liu
State Key Laboratory for Strength and Vibration of Mechanical Structures, Xi'an Jiaotong University
No. 28, Xianning West Road, 710049, Xi'an, Shaanxi, P.R. China
liuz@mail.xjtu.edu.cn

Marco Morandini
Department of Aerospace Science and Technology, Politecnico di Milano
Via La Masa 34, 20156 Milano, Italy
marco.morandini@polimi.it

Linjie Ma
State Key Laboratory for Strength and Vibration of Mechanical Structures, Xi'an Jiaotong University
No. 28, Xianning West Road, 710049, Xi'an, Shaanxi, P.R. China
malj_628@stu.xjtu.edu.cn

Pierangelo Masarati
Department of Aerospace Science and Technology, Politecnico di Milano
Via La Masa 34, 20156 Milano, Italy
pierangelo.masarati@polimi.it

ABSTRACT

The slipper is the critical component of a supersonic rocket sled that is in contact with the track. Due to clearance and contact effects, the supersonic slipper-track system displays pronounced nonlinearities. A

[1] Corresponding author.

comprehensive analysis, including bifurcation and chaos detection, is conducted on this system to predict the nonlinear behavior of the slipper. Kinematic and dynamic models of the system are established using the generalized coordinate and Lagrange multiplier methods. This model accounts for slipper-track clearances, track irregularities, and normal contact forces. The dynamic response of the slipper is examined both in time and frequency domain. The bifurcation analysis encompasses various parameters such as slipper velocity and length, and slipper-track clearance. Chaos identification is employed for both qualitative and quantitative assessments, utilizing phase diagrams, Poincaré sections, the trajectory of the slipper's center, and the largest Lyapunov exponent. The findings revealed significant nonlinear phenomena, including self-excited vibrations, super-harmonic responses, jumping phenomena, strange attractors, and combined frequencies. Notably, this study demonstrated the potential for leveraging chaotic response to mitigate the contact forces on the slipper. These insights contribute to the rationalization of control parameters and the optimization of slipper and track design.

1 Introduction

A supersonic rocket sled is a large and high-precision ground test equipment used primarily to address testing challenges encountered by aircraft operating at high speeds and in high-load factor environments [1]. Supersonic rocket sled tests utilize a rocket engine to propel the sled along a track at high velocities, concurrently evaluating the performance of a test specimen mounted on the sled. The component of the rocket sled in contact with the track is known as the "slipper". The slipper encircles the track to prevent the sled from derailing as it moves [2]. To accommodate manufacturing tolerances and installation requirements, the slippers must be slightly oversized. This clearance between the slipper and the track enables successful traversal of multiple track sections with varying dimensions, allowing the slipper to move freely both vertically and laterally. Figure 1 is a schematic diagram of a rocket sled system.

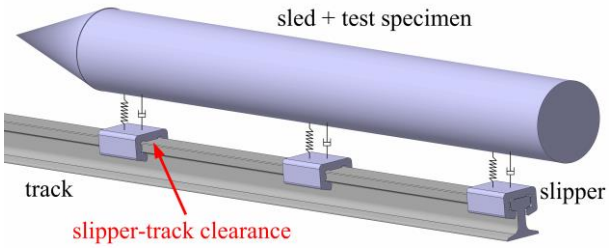

Fig. 1 Schematic diagram of rocket sled system

The presence of clearance between the slipper and the track results in a series of collisions and separations. These discontinuous contact forces can lead to an unfavorable dynamic environment for the mechanism, potentially causing the overall behavior to enter a chaotic state [3]. Consequently, the supersonic slipper-track system exhibits strong nonlinearity. Clearance nonlinearity is a discontinuous and non-differentiable function. Extensive nonlinear studies have demonstrated that even small clearances can introduce unpredictability into the system's response, resulting in reduced mechanical reliability and stability [4]. Regardless of the clearance's size, it can induce complex dynamic behaviors in mechanical systems, including bifurcation and even chaos [5]. In nonlinear systems, motion patterns can be categorized as periodic, quasiperiodic, and chaotic. Chaos arises from the interplay of global stability and local instability within the system. Local instability makes the system sensitive to initial conditions, while global stability is responsible for the emergence of certain fractal structures in the phase space. Several methods, such as phase space reconstruction, Lyapunov exponent analysis, and Poincaré section analysis, are employed to identify chaos. Quantifying chaos in the supersonic slipper-track system not only enhances our understanding of its nonlinear characteristics but also aids in rationalizing control parameters. Investigating the nonlinear dynamics of the supersonic slipper-track system is essential for predicting slipper's motion and optimizing slipper and track design, and chaos may even be harnessed to reduce contact forces on the slipper.

The supersonic slipper-track system can be essentially viewed as a specialized translational joint with clearance. Over the past few decades, scholars have undertaken extensive research into joints with clearance, encompassing the modeling of equivalent contact forces, the establishment of dynamic equations, and the active control of clearance. Most of the research has focused on revolute clearance joints [6], cylindrical clearance joints [7], and spherical clearance joints [8]. In contrast to these three types of joints with clearance, there has been relatively limited exploration of translational clearance joints. This discrepancy may arise from the complex contact modes associated with translational clearance joints [9]. As the system undergoes motion, various contact modes appear randomly. This inherent complexity poses challenges to the study of translational clearance joints.

In addressing the nonlinear dynamic equations of translational clearance joints, numerical methods are commonly employed for their resolution. The primary advantage of this approach is its ability to provide a comprehensive depiction of the system's dynamic response, encompassing main harmonic, super-harmonic, sub-harmonic, and chaotic responses. Research in this field can be categorized into two main areas: planar

translational clearance joints [9-18] and spatial translational clearance joints [19-21]. Current studies predominantly model planar translational clearance joints in a configuration resembling Fig. 2(a). Stoenescu et al. [10] investigated the dynamics of planar rigid linkages incorporating sliding joint clearances and explored the influence of driving velocity and recovery coefficients on chaotic characteristics. Flores et al. [11] formulated dynamic equations incorporating single translational clearance, comparing the effects of four clearance sizes on the mechanism. Additionally, they [12] employed multiple friction unilateral constraints to model translational clearance joints and proposed a dynamic modeling approach for crank sliders with translational clearance joints. Chen et al. [13] established rigid dynamic equations encompassing both translational and revolute clearances using the Lagrange multiplier method. Wu et al. [14] introduced the combined impact of translational and rotational clearances on the dynamics of planar rigid crank slider mechanisms, investigating correlation dimensions and bifurcations. Xiao et al. [15] considered the coupling effects of revolute clearance pairs, translational clearance pairs, and the elastic deformation of components, accurately predicting the nonlinear behavior of rigid-flexible coupling multi-link mechanisms. Furthermore, some studies explored frictional behavior in planar translational clearance joints. Xiao et al. [9] examined the stability of a coupling rub-impact system with dual translational joints, observing chaotic phenomena in phase trajectories and Poincaré sections. Zhuang et al. [16] presented a modeling and simulation method for rigid multibody systems featuring frictional translational joints, where they considered a small clearance between a slider and guide. Some scholars also treated the slider within planar translational clearance joints as a flexible body. Zhang et al. [17] introduced and discussed a finite element method for the dynamic description of multibody systems with frictional translational joints. In Zheng et al.'s study [18], the slider was discretized into finite elements, and the distributed body forces and boundary stresses (contact forces) on the slider were equated to nodal forces.

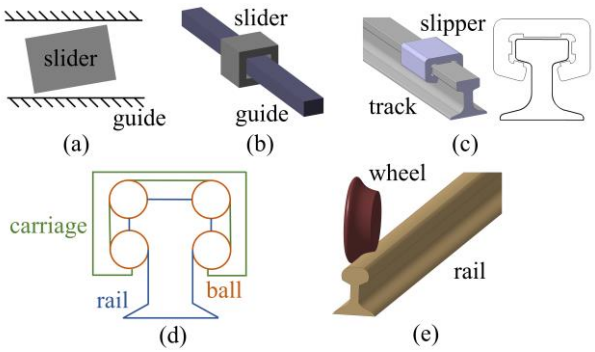

Fig. 2 Several models of systems traveling along guide rails: (a) planar translational clearance joint; (b) spatial translational clearance joint; (c) slipper-track system; (d) linear guide slide platform; (e) vehicle wheel-rail system

Spatial translational clearance joints are also referred to as prismatic clearance joints. When compared to planar translational clearance joints, the model of spatial translational clearance joints is notably more intricate. This complexity arises from the numerous contact surfaces within the components, and the contact modes are influenced by the joint's structural parameters, resulting in a greater variety of contact modes. Simultaneously, determining these contact modes under dynamic conditions presents a relatively complex challenge. Existing research typically represents spatial translational clearance joints in a configuration resembling Fig. 2(b). Wu et al. [19] introduced an enhanced model for assessing the contact forces generated by spatial translational clearance and conducted numerical investigations involving a rigid-body double crank mechanism with translational clearance. Qian et al. [20] developed a 3D model for translational joints with clearance and investigated the motion between the guide rail and slider. Qi et al. [21] proposed a methodology for the analysis of frictional contacts in rigid multibody systems featuring spatial prismatic joints. They demonstrated that all types of contacts within the joint could be transformed into point-to-point contacts, particularly suitable for cases where clearances are minimal.

As previously mentioned, existing studies on nonlinear dynamics in translational clearance joints typically represent them in the configurations depicted in Fig. 2(a) and (b). However, the model of the slipper-track system is illustrated in Fig. 2(c). While these models share the presence of clearance between joint elements and involve a collision contact mode, they differ in terms of the number of contact surfaces and the angles between them. In strongly nonlinear systems, variations in structural parameters can yield entirely distinct results. Consequently, it is not appropriate to study the slipper-track system as an equivalent to the models in Fig. 2(a) and (b).

Much like the slipper-track system, two other systems that travel along guide rails are the linear guide slide platform and the vehicle wheel-rail system. Linear guide slide platforms are commonly employed in machine tool systems such as 3D printers and sliding doors. Research on the nonlinear dynamics of linear guide slide platforms typically employs models resembling Fig. 2(d) [22-24]. Additionally, nonlinear dynamics investigations into vehicle wheel-rail systems usually use models like those in Fig. 2(e) [25-28]. In contrast to slipper-track systems, both systems lack clearances between joint elements. The contact mode in linear

guide slide platforms involves rolling between the carriage, ball, and rail, whereas the contact mode in vehicle wheel-rail systems encompasses rolling and creeping between the wheel and rail. In conclusion, while other systems traveling along guide rails can offer insights for the study of nonlinear dynamics in the slipper-track system, the establishment of a dedicated nonlinear dynamic model for the slipper-track system remains essential and irreplaceable.

Current dynamic research on supersonic slipper-track systems predominantly focuses on several key aspects, encompassing motion prediction (positions and velocities) [29-32], assessment of vibration accelerations and contact forces [30-37], and the analysis of slipper strength (stress and strain) [31,35,38,39]. This emphasis arises from the intermittent collisions between the supersonic slipper and the track during motion. On one hand, these substantial collision forces induce vibrations in both the slipper and the sled. On the other hand, they may result in slipper failures or track shear fractures. However, bifurcation analysis and chaos identification in the context of the supersonic slipper-track system have thus far been overlooked, despite their significance. The exploration of bifurcation and chaos phenomena in the supersonic slipper-track system holds importance for predicting nonlinear behaviors of the slipper, understanding the intricate interaction between the slipper and the track, and identifying key factors influencing the dynamic responses of the slipper. These findings will serve as a theoretical foundation for stability analysis and optimal slipper design, carrying scientific and engineering value. Therefore, the primary innovation of this study is to conduct a nonlinear dynamic investigation of the supersonic slipper-track system with clearance, incorporating bifurcation analysis and chaos identification to comprehend the dynamic responses of the slipper.

2 Modeling the supersonic slipper-track system

2.1 Kinematic model of slipper-track system

As the primary focus of this study centers on elucidating nonlinear phenomena arising from clearance and understanding the interaction between the slipper and the track, we have opted not to establish an analysis model for the rocket sled. Instead, we have devised a three-dimensional analysis model for the slipper-track system, as depicted in Fig. 3. In this model, the slipper and the track are represented by subscript S and T respectively. The length of the slipper is denoted as L_S. The slipper node, localized within its own coordinate system O_S-$x_S y_S z_S$, possesses initial velocities in three directions and initial angular velocities in three directions as well. Furthermore, the slipper's traveling velocity V_X remains constant throughout the

computational analysis. The slipper element is characterized by mass M and moments of inertia $\mathbf{J}$. To facilitate the modeling of the contact relationship between the slipper and the track, the concept of track nodes is introduced. Track nodes, which do not exist in actual track structures, are devoid of mass and inertia but possess motion properties. Two track nodes are positioned on both the front and rear sides of the slipper. These track nodes, both equipped with their own local coordinate system (O_{1T}-x_{1T} y_{1T} z_{1T} and O_{2T}-x_{2T} y_{2T} z_{2T}), are on the principal axis of the track and follow the traveling movement of the slipper node. All six degrees of freedom for the track nodes are constrained. Specifically, in the x direction, relative position constraints are imposed with respect to the slipper node, while in the y and z directions, and in the orientation along the x direction, constraints are anchored to track irregularities. The orientations in the y and z directions are constrained to the ground node, representing the global coordinate system O-xyz.

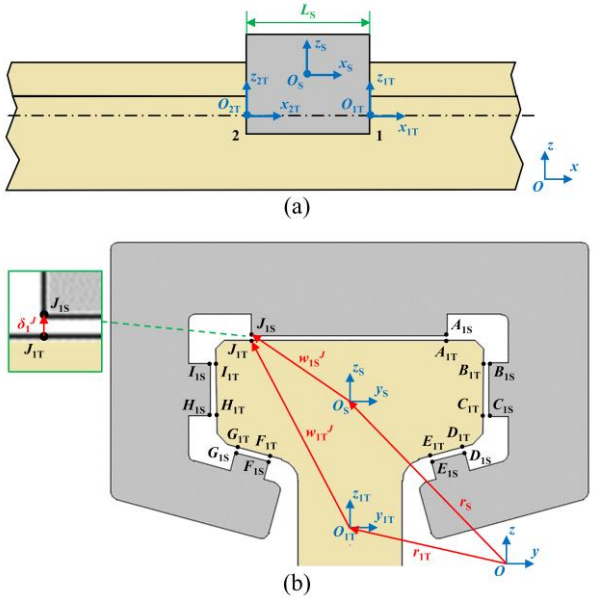

Fig. 3 Analysis model for slipper-track system: (a) xz-plane; (b) yz-plane

Both the slipper and the track are considered rigid. Consequently, when the slipper contacts the track, the contact points on the slipper inevitably encompass all 20 of its corners, specifically identified as A_{1S} to J_{1S} and A_{2S} to J_{2S}. This study exclusively employs point-to-point contact definitions and refrains from utilizing surface-to-surface contacts. This approach is adopted because, even if surface-to-surface contacts were to occur, all four corners of the slipper's contact surface engage with the track. Qi et al. [21] have demonstrated that all types of contacts within translational clearance joints can be effectively converted into point-to-point contacts, which is particularly well-suited for situations involving minimal clearances. Points A_{1T} to J_{1T} and

A_{2T} to J_{2T} represent the locations on the track nearest to the corners of the slipper. To provide a detailed modeling and analysis example, this study focuses on points J_{1S} and J_{1T}, as illustrated in Fig. 3(b). The global coordinates of points J_{1S} and J_{1T} are

$$\begin{cases} \mathbf{r}_{1S}^{J} = \mathbf{r}_{S} + \mathbf{R}_{S}\mathbf{w}_{1S}^{J} \\ \mathbf{r}_{1T}^{J} = \mathbf{r}_{1T} + \mathbf{R}_{1T}\mathbf{w}_{1T}^{J} \end{cases}, \tag{1}$$

where, $\mathbf{r}_S$ and $\mathbf{r}_{1T}$ are global coordinates of the slipper node O_S and the track node O_{1T}. $\mathbf{w}_{1S}^{J}$ and $\mathbf{w}_{1T}^{J}$ are position vectors of points J_{1S} and J_{1T}. $\mathbf{R}_S$ and $\mathbf{R}_{1T}$ are rotational transformation matrices of the slipper node O_S and the track node O_{1T}. Take $\mathbf{R}_S$ as an example. $\mathbf{R}_S$ is defined with Euler angles in three directions, namely the roll angle ϕ_S, the pitch angle φ_S, and the yaw angle γ_S, and is evaluated by

$$\mathbf{R}_S = \begin{pmatrix} \cos(\gamma_S) & -\sin(\gamma_S) & 0 \\ \sin(\gamma_S) & \cos(\gamma_S) & 0 \\ 0 & 0 & 1 \end{pmatrix} \begin{pmatrix} \cos(\varphi_S) & 0 & \sin(\varphi_S) \\ 0 & 1 & 0 \\ -\sin(\varphi_S) & 0 & \cos(\varphi_S) \end{pmatrix} \begin{pmatrix} 1 & 0 & 0 \\ 0 & \cos(\phi_S) & -\sin(\phi_S) \\ 0 & \sin(\phi_S) & \cos(\phi_S) \end{pmatrix}. \tag{2}$$

The position vector from point J_{1T} to point J_{1S} can be expressed as

$$\boldsymbol{\delta}_1^J = \mathbf{r}_{1S}^J - \mathbf{r}_{1T}^J . \tag{3}$$

For points on the track surface, the position vector from point J_{1T} to point A_{1T} can be denoted as $(\mathbf{r}_{1T}^A - \mathbf{r}_{1T}^J)$, while the position vector from point J_{1T} to point J_{2T} can be denoted as $(\mathbf{r}_{2T}^J - \mathbf{r}_{1T}^J)$. Both vectors are orthogonal to the unit normal vector $\mathbf{n}_1^J$ of the track surface, passing through point J_{1T}. Therefore, $\mathbf{n}_1^J$ can be expressed as

$$\mathbf{n}_1^J = \frac{(\mathbf{r}_{1T}^A - \mathbf{r}_{1T}^J) \times (\mathbf{r}_{2T}^J - \mathbf{r}_{1T}^J)}{\left\| (\mathbf{r}_{1T}^A - \mathbf{r}_{1T}^J) \times (\mathbf{r}_{2T}^J - \mathbf{r}_{1T}^J) \right\|} . \tag{4}$$

The condition of collision between point J_{1S} and point J_{1T} can be denoted as

$$(\mathbf{n}_1^J)^{\mathrm{T}} \cdot \boldsymbol{\delta}_1^J \le 0 . \tag{5}$$

The normal contact force is determined by calculating the penetration depth and the relative normal velocity. Specifically, the penetration depth at point J_{1S} can be expressed as

$$\delta_1^J = \sqrt{(\boldsymbol{\delta}_1^J)^{\mathrm{T}} \cdot \boldsymbol{\delta}_1^J} . \tag{6}$$

The global velocities of points J_{1S} and J_{1T} are

$$\begin{cases} \dot{\mathbf{r}}_{1S}^{J} = \dot{\mathbf{r}}_{S} + \dot{\mathbf{R}}_{S}\mathbf{w}_{1S}^{J} \\ \dot{\mathbf{r}}_{1T}^{J} = \dot{\mathbf{r}}_{1T} + \dot{\mathbf{R}}_{1T}\mathbf{w}_{1T}^{J} \end{cases}, \tag{7}$$

where the dot represents the time derivative.

The relative normal velocity between point J_{1T} and point J_{1S} is given by

$$\dot{\delta}_{1}^{J} = (\dot{\mathbf{r}}_{1S}^{J} - \dot{\mathbf{r}}_{1T}^{J})^{T} \cdot \mathbf{n}_{1}^{J} . \tag{8}$$

The modeling approach for the remaining contact points is analogous to that of point *J*. For reference, the relative positions of each contact point and the slipper node are detailed in Table 1.

Table 1 Relative positions of each contact point and slipper node

Point	*y* / m	*z* / m
A	0.03	0.013
B	0.048	0.0055
C	0.048	-0.0145
D	0.0445	-0.0249
E	0.029	-0.029
F	-0.029	-0.029
G	-0.0445	-0.0249
H	-0.048	-0.0145
I	-0.048	0.0055
J	-0.03	0.013

As mentioned earlier, positions of track nodes in the *y* and *z* directions, as well as the rotational orientation about the *x*-axis, are constrained due to track irregularities. These irregularities typically arise from manufacturing and assembly errors, constituting the primary cause of contact between the slipper and the track [38]. Given that track irregularities exhibit random patterns in the frequency domain, their energy typically encompasses multiple frequency components. Consequently, the dynamic response of the slipper comprises various frequency components and their nonlinear combinations. Isolating the influence of each frequency of irregularities on the slipper's dynamic responses during analysis can be challenging. Therefore, the conventional approach involves initially simplifying irregularities into a single-frequency simple harmonic function and subsequently modeling them as functions containing dual frequencies or multiple frequencies [29]. This study also adopts this approach, accounting for track irregularities in the *y* and *z* directions, as well as rotational orientation about the *x*-axis. For rocket sled tracks, actual measured values of the dominant irregularity wavelengths are generally in the range of 5 m to 30 m. The wavelength of these track irregularities is denoted as L_X, leading to an expression for the frequency of track irregularities as

$$f_{T} = V_{X} / L_{X} . \tag{9}$$

Irregularities of track node O_{1T} in the above three directions with respect to time t can be expressed as

$$\begin{cases} P_Y^{1T} = \mathrm{Amp} \cdot \sin(2\pi f_T t) \\ P_Z^{1T} = \mathrm{Amp} \cdot \sin(2\pi f_T t) \\ E_X^{1T} = \mathrm{Amp}_R \cdot \sin(2\pi f_T t) \end{cases}, \tag{10}$$

where Amp is the amplitude of track irregularities in the y and z directions, and Amp_R is the rotational amplitude of track irregularity in the x direction. Track irregularities of track node O_{2T} can be expressed as

$$\begin{cases} P_Y^{2T} = \mathrm{Amp} \cdot \sin[2\pi f_T (t - L_S / V_X)] \\ P_Z^{2T} = \mathrm{Amp} \cdot \sin[2\pi f_T (t - L_S / V_X)] \\ E_X^{2T} = \mathrm{Amp}_R \cdot \sin[2\pi f_T (t - L_S / V_X)] \end{cases}, \tag{11}$$

where L_S is the length of slipper.

2.2 Dynamic model of slipper-track system

An ideal spatial translational joint reduces five degrees of freedom of a system, comprising translation in two directions and rotation in three directions. However, the introduction of clearance eliminates these five motion constraints on the slipper and introduces 20 point-to-point contact force constraints. There are two primary approaches for modeling contact events: the non-smooth approach and the penalty method [40]. In contrast to non-smooth methods, penalty methods are known for their simplicity, computational efficiency, and ease of implementation [41]. Penalty models establish contact forces as continuous functions of the relative penetration (and its temporal derivative) of the deformable contacting bodies [42]. In this study, among the numerous penalty models available, we have adopted the method proposed by Flores et al. [43]. This contact force model bears similarities to the models proposed by Hunt and Crossley [44] and Lankarani and Nikravesh [45]. However, in the latter two models, the hysteresis damping factors for a perfectly plastic contact are not infinite, as might be expected. The model proposed by Flores et al. successfully addresses this issue. Taking points J_{1S} and J_{1T} as examples, the normal contact force in the model proposed by Flores et al. can be expressed as

$$\begin{cases} F_{1J} = 0 & \delta_1^J \geq 0 \\ F_{1J} = K \left| \delta_1^J \right|^e [1 + \dfrac{8(1 - c_r)}{5c_r} \dfrac{\dot{\delta}_1^J}{\dot{\delta}_1^{J(-)}}] & \delta_1^J < 0 \end{cases}, \tag{12}$$

where K represents the generalized stiffness parameter, and the exponent e is typically equal to 3/2. The coefficient of restitution c_r quantifies the ratio of relative velocity between two colliding points after and

before impact, falling within the range [0, 1]. Additionally, $\dot{\delta}_1^{J(-)}$ denotes the initial contact velocity between points J_{1S} and J_{1T}.

From Eq. (12), it is evident that the contact force exhibits nonlinearity concerning relative position and velocity. Consequently, the supersonic slipper-track system incorporates nonlinearity due to both clearance and contact, leading to the presence of significant nonlinearity in its dynamic equations. Furthermore, the contact force model considers energy dissipation during contact, which creates conditions for the nonlinear slipper-track system to exhibit self-excited behavior. In this system, the slipper's constant traveling velocity V_X serves as the sole parameter continuously supplying energy to the system, while contact between the slipper and the track results in energy dissipation. Under specific physical parameters, the system's inherent regulation can lead to energy alternation. When the input and dissipated energy reach equilibrium, the system can sustain vibrations with a constant amplitude, and the dynamic responses of the slipper can exhibit evident periodic behavior.

The dynamic modeling and computation of the supersonic slipper-track system are performed using MBDyn, a multibody/multiphysics analysis program developed at the Department of Aerospace Science and Technology, Politecnico di Milano [46,47]. Since the analysis of the supersonic slipper-track system involves solving an initial value problem (IVP), the constrained dynamic equations are formulated as

$$\begin{cases} \mathbf{M}\dot{\mathbf{x}} - \boldsymbol{\beta} = \mathbf{0} \\ \dot{\boldsymbol{\beta}} + \boldsymbol{\Phi}_{/\mathbf{x}}^{\mathrm{T}}\boldsymbol{\lambda}_{\boldsymbol{\Phi}} + \boldsymbol{\Psi}_{/\dot{\mathbf{x}}}^{\mathrm{T}}\boldsymbol{\lambda}_{\boldsymbol{\Psi}} = \mathbf{f}(\mathbf{x}, \dot{\mathbf{x}}, t) \\ \boldsymbol{\Phi}(\mathbf{x}, t) = \mathbf{0} \\ \boldsymbol{\Psi}(\mathbf{x}, \dot{\mathbf{x}}, t) = \mathbf{0} \end{cases}, \tag{13}$$

where $\mathbf{M}$ represents the generalized mass matrix, $\mathbf{x}$ stands for the vector of generalized coordinates, $\boldsymbol{\beta}$ denotes the vector of generalized momenta, and $\boldsymbol{\Phi}_{/\mathbf{x}}$ and $\boldsymbol{\Psi}_{/\dot{\mathbf{x}}}$ are the Jacobian matrices of the constraints. The operator $(\cdot)_{/\mathbf{x}}$ indicates partial derivative with respect to $\mathbf{x}$, and $\boldsymbol{\lambda}_{\boldsymbol{\Phi}}$ and $\boldsymbol{\lambda}_{\boldsymbol{\Psi}}$ represent the Lagrange multipliers associated with holonomic and nonholonomic constraint equations. The vector $\mathbf{f}$ encompasses generic forces and moments. The final two rows of Eq. (13) are algebraic equations that express the kinematic constraints of the supersonic slipper-track system. The detailed formulation of Eq. (13) is given in Appendix A1. Consequently, Eq. (13) can be formulated as a system of implicit Differential-Algebraic Equations (DAE)

$$\mathbf{r}(\mathbf{x}, \dot{\mathbf{x}}, t) = \mathbf{0} \tag{14}$$

integrated in time using implicit A/L stable linear multistep integration schemes, which can be expressed as

$$\mathbf{x}_k = \sum_{i=1}^{2} a_i \mathbf{x}_{k-i} + h \sum_{i=0}^{2} b_i \dot{\mathbf{x}}_{k-i} \,, \tag{15}$$

where a_i and b_i represent the coefficients, while h stands for the step size. The perturbation of Eq. (15) is denoted as

$$\partial \mathbf{x}_k = h b_0 \partial \dot{\mathbf{x}}_k \,. \tag{16}$$

Therefore, the linearization of Eq. (13), which is necessary for the Newton-like iterative solution process, yields

$$\begin{bmatrix} \mathbf{M} & -hb_0\mathbf{I} & \mathbf{0} & \mathbf{0} \\ -(hb_0\mathbf{f}_{/\mathbf{x}} + \mathbf{f}_{/\dot{\mathbf{x}}}) & \mathbf{I} & \boldsymbol{\Phi}_{/\mathbf{x}}^{\mathrm{T}} & \boldsymbol{\Psi}_{/\dot{\mathbf{x}}}^{\mathrm{T}} \\ \boldsymbol{\Phi}_{/\mathbf{x}} & \mathbf{0} & \mathbf{0} & \mathbf{0} \\ \boldsymbol{\Psi}_{/\dot{\mathbf{x}}} & \mathbf{0} & \mathbf{0} & \mathbf{0} \end{bmatrix} \begin{Bmatrix} \partial \dot{\mathbf{x}} \\ \partial \dot{\boldsymbol{\beta}} \\ \partial \boldsymbol{\lambda}_{\boldsymbol{\Phi}} \\ \partial \boldsymbol{\lambda}_{\boldsymbol{\Psi}} \end{Bmatrix} = RHS \,. \tag{17}$$

To solve the dynamic model of the supersonic slipper-track system, MBDyn computes the derivatives of the model's state initially and then proceeds with the first step and subsequent ones. The first step requires a self-starting integration scheme, for which the Crank-Nicolson formula, as defined in Eq. (15) with $a_1 = 1$, $b_0 = b_1 = 1/2$, and $a_2 = b_2 = 0$, is utilized. It is important to note that this method is unconditionally stable and offers second-order accuracy. However, it is not well-suited for the integration of DAEs as it does not introduce any algorithmic dissipation. Nevertheless, in this specific context it is only employed for one step. Subsequent steps are executed using an A/L stable linear multistep algorithm formulated according to Eq. (15). The coefficients are chosen to ensure second-order accuracy and to align the asymptotic roots of the characteristic polynomial

$$(1 - h\lambda b_0)\rho^2 - (a_1 + h\lambda b_1)\rho - (a_2 + h\lambda b_2) = 0 \tag{18}$$

with $|h\lambda| \to \infty$, converging to a specified value $|\rho_\infty|$ when addressing a purely oscillatory problem $\dot{x} = \lambda x = \mathrm{j}\omega x$. This feature enables the adjustment of algorithmic dissipation, and the resulting coefficients are denoted as

$$\begin{cases} a_1 = 1-\beta \\ a_2 = \beta \\ b_0 = \chi/\alpha + \alpha/2 \\ b_1 = \beta/2 + \alpha/2 - (1+\alpha)\chi/\alpha \\ b_2 = \beta/2 + \chi \end{cases} \tag{19}$$

with

$$\begin{cases} \alpha = \dfrac{t_k - t_{k-1}}{t_{k-1} - t_{k-2}} \\ \beta = \alpha \dfrac{(2+\alpha)(1-|\rho_\infty|)^2 + 2(1+\alpha)(2|\rho_\infty|-1)}{2(1+\alpha)-(1-|\rho_\infty|)^2}, \\ \chi = \dfrac{\alpha^2(1-|\rho_\infty|)^2}{2(2(1+\alpha)-(1-|\rho_\infty|)^2)} \end{cases} \tag{20}$$

where A-stability (unconditional stability) can be obtained by choosing $0 \le |\rho_\infty| \le 1$.

The parameters for the dynamic model are provided in Table 2. Specifically, f_T represents the frequency of track irregularities, which is associated with the traveling velocity V_X of the slipper according to Eq. (9). Consequently, in the calculations for different traveling velocities, the integral step size varies accordingly.

Table 2 Parameters for dynamic model

Parameter	Value
Initial slipper velocity V_Y	0.5 m s^{-1}
Initial slipper velocity V_Z	0.5 m s^{-1}
Initial slipper angular velocity ω_X	0.2 rad s^{-1}
Initial slipper angular velocity ω_Y	0.3 rad s^{-1}
Initial slipper angular velocity ω_Z	0.4 rad s^{-1}
Mass of slipper M	14 kg
Inertia of slipper J_X	0.051 kg m^2
Inertia of slipper J_Y	0.060 kg m^2
Inertia of slipper J_Z	0.086 kg m^2
Contact stiffness K	10^8 N m$^{-1.5}$
Coefficient of restitution c_r	0.9
Wavelength of track irregularity L_X	8 m
Amplitude of track irregularity Amp	1 mm
Rotational amplitude of track irregularity Amp$_R$	0.2 degrees
Integral tolerance	10^{-6}
Integral step	0.001/f_T

3 Results and discussions

In this section, we explore the effects of various parameters on the nonlinear dynamic responses of the slipper. These parameters include the traveling velocity of the slipper V_X, slipper-track clearance value C,

and length of the slipper L_S. We examine these effects individually when track irregularities are represented as a single-frequency function. Our analysis involves bifurcation analysis of the responses resulting from these parameters and quantitative chaos identification using the largest Lyapunov exponent (LLE). Furthermore, we discuss the nonlinear dynamic responses of the slipper when track irregularities are characterized as a dual-frequency function. It is important to note that in this study, when referring to the rotations of the slipper in three directions, the roll direction corresponds to the *x*-axis, the pitch direction to the *y*-axis, and the yaw direction to the *z*-axis.

3.1 Traveling velocity of slipper

We examine the dynamic responses of the slipper at different traveling velocities V_X – specifically, at 900 m s^{-1}, 1500 m s^{-1}, and 2300 m s^{-1}, while keeping slipper-track clearance value C = 1 mm and length of slipper L_S = 0.2 m. We analyze the roll angular accelerations α_x over time, their power spectral density (PSD), and present phase diagrams and Poincaré portraits (depicted as red points) in Fig. 4. From Fig. 4(a) and (b), it is evident that the slipper-track system exhibits self-excited vibrations at stable traveling velocities of V_X = 900 m s^{-1} and 1500 m s^{-1}, displaying clear periodicity in its responses. It is worth noting that since the wavelength of track irregularity, L_X, remains constant in this study, variations in the traveling velocity V_X of the slipper are equivalent to changes in the frequency f_T of the track irregularity, as per Eq. (9). Figure 4(a) shows that the time waveform repeats itself at intervals of $3/f_T$, reflecting that the energy of angular acceleration concentrates at two distinct frequencies, f_T and $2f_T/3$. A super-harmonic response appears in the spectrum of Fig. 4(b). In nonlinear systems, the amplitude corresponding to each frequency multiplication is influenced by system damping. In this case, damping arises from the energy dissipation during slipper-track contact. Consequently, the energy associated with frequency multiplications $2f_T$ and $3f_T$ is reduced, resulting in the time waveform repeating at intervals of $1/f_T$. Moving on to Fig. 4(c), we observe chaotic behavior, where the time domain plot loses its periodicity, and the frequency domain plot exhibits a continuous spectrum. Interestingly, the main frequency of the response is no longer the frequency f_T of the track irregularity but rather $2f_T/5$. Additionally, the qualitative determination of periodic or chaotic behavior can be made through phase diagrams and Poincaré maps. Typically, to assess whether a system exhibits chaotic behavior through the Poincaré section, we rely on the following criteria: (1) A Poincaré section with one or several discrete fixed points suggests periodic motion; (2) A closed curve in the Poincaré section indicates quasiperiodic motion; (3) A Poincaré section with a group of densely distributed points forming fractal structures suggests

chaotic behavior. Considering these criteria, Fig. 4(a) corresponds to period-2 motion, where the phase trajectory completes two loops and intersects the Poincaré section twice. As the slipper's traveling velocity increases, the phase trajectory changes. In Fig. 4(b), we observe period-1 motion, where the phase trajectory is approximately circular, and the Poincaré section has only one point. Finally, Fig. 4(c) illustrates chaotic motion, characterized by irregular phase trajectories and a Poincaré section displaying a two-dimensional fractal pattern. This fractal structure showcases limited range and infinite details.

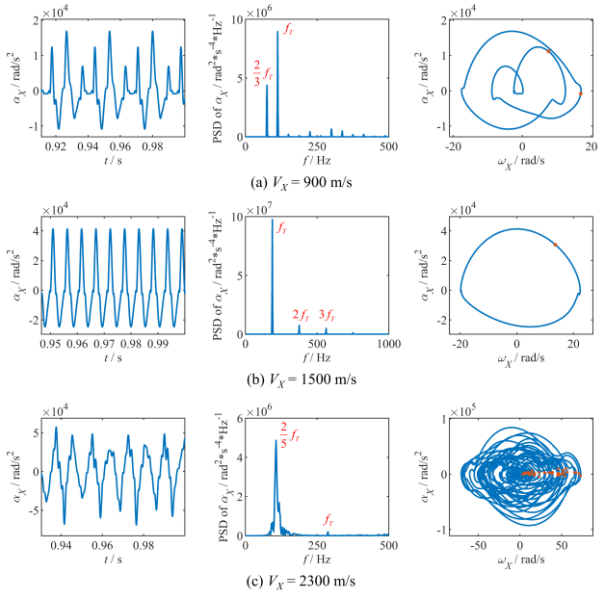

Fig. 4 Dynamic responses of slipper at various traveling velocities: (a) V_X = 900 m s^{-1}; (b) V_X = 1500 m s^{-1}; (c) V_X = 2300 m s^{-1}

To analyze the chaotic characteristics of the slipper-track system in relation to the traveling velocity V_X, we conducted a bifurcation analysis, illustrated in Fig. 5. The horizontal axis of Fig. 5 represents 241 traveling velocities ranging linearly from 100 m s^{-1} to 2500 m s^{-1}, while the vertical axis represents the velocities or angular velocities corresponding to the Poincaré section at each traveling velocity. These include lateral velocity V_Y, vertical velocity V_Z, roll angular velocity ω_X, pitch angular velocity ω_Y, and yaw angular velocity ω_Z. As per Eq. (9), the traveling velocity V_X of the slipper and the frequency f_T of track irregularity are linearly and positively correlated. Thus, the linear increase in slipper traveling velocity is equivalent to a forward linear frequency sweep due to track irregularities, with the sweep speed approaching zero. In the bifurcation diagram of lateral velocity V_Y, it can be observed that at traveling velocity V_X = 820 m s^{-1}, the lateral motion of the slipper transitions from chaotic to period-3 behavior. This period-3 motion shifts to

period-1 as traveling velocity increases to 980 m s^{-1} and remains in that state until V_X = 1810 m s^{-1}. Within this range, the lateral velocity continues to rise with traveling velocity, indicating this range is the resonance zone within the system. However, at V_X = 1810 m s^{-1}, a jumping phenomenon occurs, causing the lateral velocity to drop sharply, and the lateral motion shifts from self-excited vibration to attenuated vibration. This jump corresponds to a phase space transformation from an unstable focus accompanied by a limit cycle to a stable focus, known as Hopf bifurcation. This discontinuous jump demonstrates the system's nonlinearity. The bifurcation diagram for vertical velocity V_Z exhibits similar characteristics to lateral velocity. However, within the range of V_X = 820 ~ 980 m s^{-1}, the vertical motion of the slipper is period-2. As the traveling velocity increases, the slipper transitions through chaotic, period-1, chaotic, period-2, period-1, and chaotic motion in the roll direction. Notably, within the V_X = 1660 ~ 1810 m s^{-1} range, the roll angular velocity ω_X does not intersect with the selected Poincaré section (roll angle ϕ_S = 0 degrees), indicating that the slipper consistently tilts to one side of the track. This could potentially lead to tilting or derailing of the rocket sled during tests. The bifurcation patterns for pitch angular velocity ω_Y and yaw angular velocity ω_Z are similar to that of roll angular velocity ω_X. All three exhibit the possibility of very large angular velocities when the traveling velocity V_X of the slipper exceeds 1810 m s^{-1}.

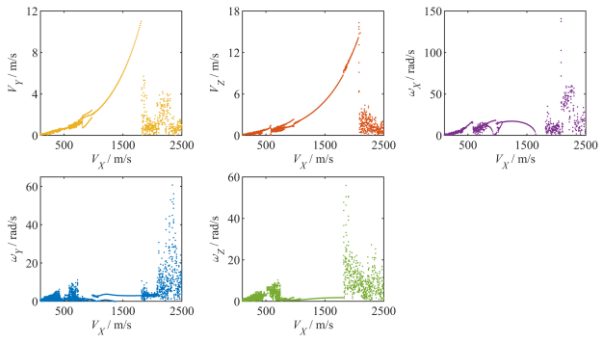

Fig. 5 Bifurcation diagrams concerning traveling velocity of slipper

To quantitatively assess the chaotic responses of the slipper, we conducted chaos identification using the LLE. Among various numerical characteristics used to identify chaotic motion, the Lyapunov exponent serves as an indicator of the average exponential divergence rate of adjacent trajectories within the phase space. For a one-dimensional system

$$x_{n+1} = f(x_n), \tag{21}$$

the Lyapunov exponent can be expressed as [48]

$$\lambda = \lim_{n\to\infty} \frac{1}{n} \sum_{n=0}^{n-1} \ln \left| \frac{\mathrm{d}f(x_n)}{\mathrm{d}x} \right|, \tag{22}$$

where n denotes the number of iterations. For an m-dimensional phase space, there are m Lyapunov exponents. The LLE can be represented as

$$\mathrm{LLE} = \max(\lambda_1, \lambda_2, ..., \lambda_m) . \tag{23}$$

In assessing the chaotic nature of a system, the presence of at least one positive Lyapunov exponent indicates chaos. The LLE is a useful metric for determining the system's behaviors: when LLE is greater than zero, the system exhibits chaotic motion; when LLE equals zero, the system is stable; when LLE is less than zero, the system displays periodic motion. Furthermore, a higher LLE value corresponds to a greater degree of chaos within the system. Figure 6 depicts the relation between the LLE and the slipper's traveling velocity V_X. When the traveling velocity is below 850 m s^{-1}, the system predominantly exhibits chaotic behavior. Within the narrow range of V_X = 480 ~ 490 m s^{-1}, periodic motion occurs. At V_X = 850 m s^{-1}, LLE reaches zero. At this point, the system's attractor transitions to a limit cycle, and the ensuing periodic motion is solely determined by the physical parameters of the system, independent of the initial conditions of the slipper. As the traveling velocity continues to increase, the slipper alternates between periodic and chaotic motion. For traveling velocities exceeding 1810 m s^{-1}, the system consistently demonstrates chaotic behavior.

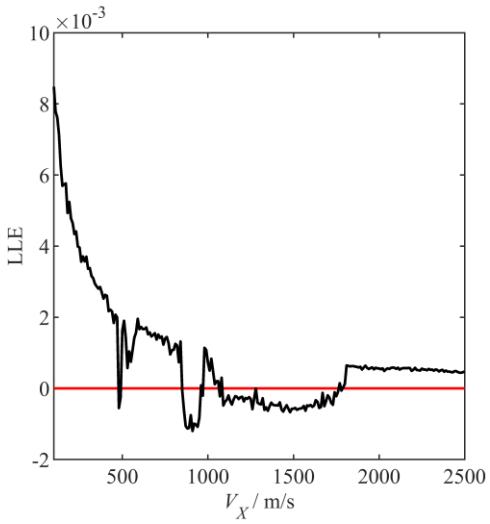

Fig. 6 LLE vs. traveling velocity of slipper

3.2 Slipper-track clearance value

We examined the dynamic responses of the slipper for two different slipper-track clearance values: 1 mm and 4 mm, while keeping traveling velocity of slipper V_X = 1250 m s^{-1} and length of slipper L_S = 0.2 m. In Fig. 7, we present the trajectories of the slipper's center in the *yz*-plane, along with phase diagrams and Poincaré portraits for the *y* and *z* directions. For a clearance value of C = 1 mm, the trajectory of the slipper's center exhibits periodic behavior. Conversely, when C = 4 mm, the periodicity is lost, but the trajectory maintains a similar shape to the former case. By analyzing the system's dynamic responses in discrete phase space, we can further explore the impact of clearance size on the system. In Fig. 7(a), both the *y* and *z* phase trajectories form closed loops, and isolated Poincaré points are observed, indicating period-1 motion. Even when we vary the initial conditions of the slipper, the phase trajectories and Poincaré sections remain consistent, reflecting the self-excited vibration characteristics of the system. This behavior is expected in self-excited vibrations, as the frequency and amplitude are primarily determined by the system's physical parameters and remain independent of initial conditions. In Fig. 7(b), the phase trajectories exhibit patterns similar to period-1 motion, suggesting that the slipper exhibits similar dynamic characteristics across different clearance values. However, with a clearance value of C = 4 mm, the phase trajectories no longer form closed loops; instead, they become separated and entangled with a finite width. The attractors shift from fixed points to strange attractors. As the clearance value increases, the phase diagram areas expand, and the corresponding Poincaré maps diffuse. The points on the Poincaré sections form lines, indicating that the system undergoes quasiperiodic motion.

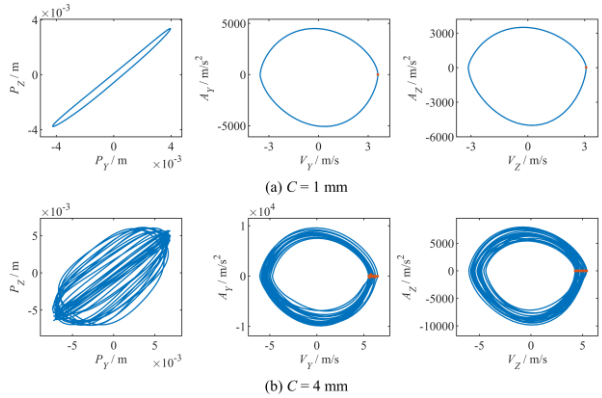

Fig. 7 Dynamic responses of slipper at various clearance values: (a) C = 1 mm; (b) C = 4 mm

We employed the bifurcation diagrams to investigate the impact of the slipper-track clearance value C on the chaotic responses of the slipper, as illustrated in Fig. 8. The horizontal axis encompasses 197 clearance

values, linearly ranging from 0.1 mm to 5 mm, while the vertical axis represents the velocities and angular velocities corresponding to each clearance value in the Poincaré sections. For a specific clearance value, we characterized 10 end periods, reflecting steady-state behaviors, in the bifurcation diagrams. From Fig. 8, when the clearance value C is less than 2.575 mm, all the velocities and angular velocities of the slipper increase as the clearance value rises, indicating that larger clearances intensify collisions between the slipper and the track. Therefore, for the purpose of vibration reduction, it is advisable to design a smaller slipper-track clearance. Within this range, the system's responses predominantly exhibit periodic behaviors. However, a notable exception occurs at C = 1.675 mm, where the slipper's responses bifurcate momentarily but then return to periodicity. Furthermore, it is noteworthy that the pitch angular velocity ω_Y transitions from period-1 motion to period-2 motion at a clearance value of C = 0.6 mm, while other dynamic responses maintain period-1 motion. In summary, the system experiences bifurcation at C = 2.575 mm and remains in a chaotic state thereafter. As the clearance value increases, the number of bifurcations gradually rises, indicating a growing prevalence of chaotic behavior in the system. Notably, the dense distribution area of the roll angular velocity ω_X extends progressively towards the horizontal axis.

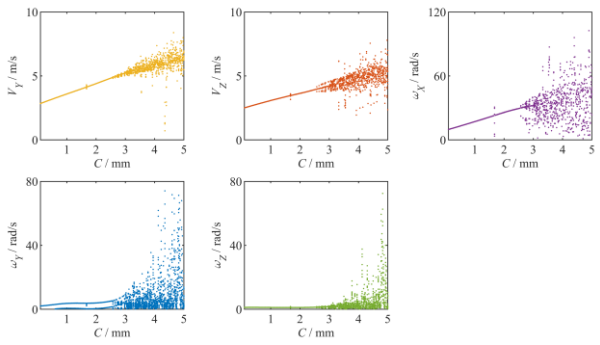

Fig. 8 Bifurcation diagrams concerning slipper-track clearance value

The range of chaotic responses influenced by the slipper-track clearance value C is determined through LLE, as depicted in Fig. 9. LLE generally increases with the clearance value, albeit with some fluctuations. This trend indicates that a larger clearance corresponds to a less periodic response of the system, aligning with the results of the bifurcation analysis. Notably, when the clearance value is C = 1.675 mm, a local positive LLE emerges, signifying an unstable motion state of the slipper. At C = 2.15 mm, LLE equals zero. At this specific clearance value, the phase trajectory of the slipper forms an isolated closed loop, indicative of a limit cycle. However, at C = 2.575 mm, LLE increases sharply, reaching a positive value, and the system

exhibits chaotic characteristics. At this clearance value, the behavior of the supersonic slipper-track system becomes uncertain, non-repetitive, and unpredictable. Therefore, from a predictability standpoint, it is also advisable to design a smaller slipper-track clearance.

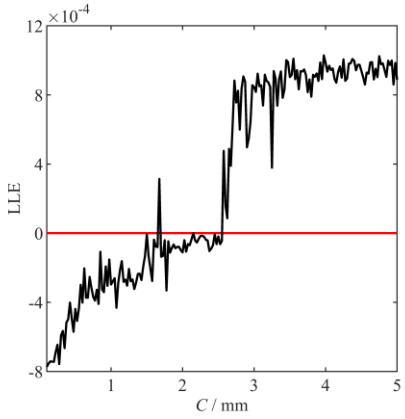

Fig. 9 LLE vs. slipper-track clearance value

3.3 Length of slipper

The length of the slipper is another critical bifurcation factor that requires careful consideration. This study explores 161 slipper lengths linearly distributed in the range from 0.1 m to 0.5 m to examine the system's periodicity, while keeping traveling velocity of slipper V_X = 1250 m s^{-1} and slipper-track clearance value C = 1 mm. The bifurcation diagrams concerning the slipper's length L_S are presented in Fig. 10. Five velocities or angular velocities of the slipper exhibit a consistent bifurcation pattern at a length of 0.15 m. When the slipper's length L_S is less than 0.15 m, the system's dynamic behavior becomes unpredictable. However, when slipper's length L_S exceeds 0.15 m, clustered points indicate that the dynamic responses of the slipper become periodic. Furthermore, the lateral velocity V_Y and vertical velocity V_Z of the slipper remain stable within this range and do not vary with the slipper's length. Regarding the roll angular velocity ω_X, it remains mostly stable except for a slight dip in the range of L_S = 0.1975 m to 0.2275 m. From a broader perspective, during chaotic motion, the pitch angular velocity ω_Y and yaw angular velocity ω_Z of the slipper are considerably higher than during periodic motion. Additionally, unlike other responses, the pitch angular velocity ω_Y shifts from period-1 motion to period-2 motion in the range of L_S = 0.1975 m to 0.2275 m.

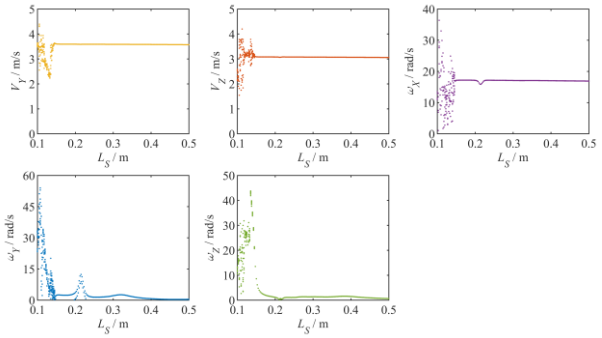

Fig. 10 Bifurcation diagrams concerning length of slipper

To confirm the chaotic characteristics observed in Fig. 10, the LLE method is employed, as illustrated in Fig. 11. When the slipper's length L_S is less than 0.15 m, the LLE is greater than zero. This signifies that, regardless of how slight the system is perturbed at its initial state, the distance between the new motion trajectory and the original one increases exponentially over time, rendering it unpredictable. At an L_S of 0.15 m, the LLE experiences a sharp decline, transitioning the system from a chaotic state to a periodic one. For slipper's length L_S exceeding 0.15 m, the LLE consistently remains negative, albeit with fluctuations. This implies that the corresponding system's motion state stabilizes over time and becomes insensitive to its initial conditions. In summary, both the bifurcation diagram and the LLE method yield concordant results in determining whether the system is chaotic or periodic. However, the LLE value offers the added advantage of quantifying the degree of chaos within the system.

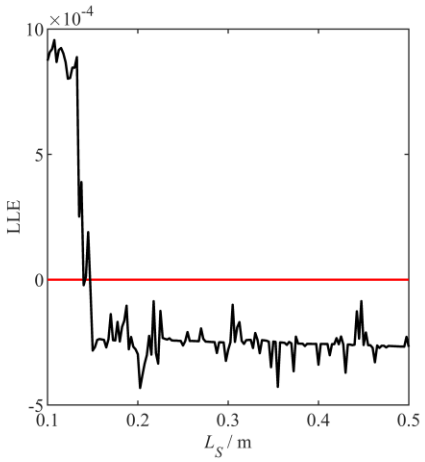

Fig. 11 LLE vs. length of slipper

The normal contact forces on the slipper are also factors that need to be considered, as excessive contact forces may damage the slipper. Figure 12 displays the time history of normal contact forces for slipper lengths

of L_S = 0.1 m and L_S = 0.4 m, respectively. The contact points shown are A_{2S}, C_{2S}, and J_{2S}. As per the earlier analysis, slipper motion is chaotic at L_S = 0.1 m, resulting in non-periodic contact forces at each point. Conversely, the slipper motion is periodic at L_S = 0.4 m, leading to periodic contact forces. In Fig. 12(a), the maximum contact force values at the three points are 1977 N, 8807 N, and 5447 N, respectively. However, Fig. 12(b) reveals maximum contact force values of 4256 N, 12824 N, and 20365 N at the same three points. A comparison shows that the normal contact forces on the slipper when its length is L_S = 0.1 m are considerably smaller than those when its length is L_S = 0.4 m. This pattern extends to other contact points not shown. The underlying reason why contact forces on the slipper during chaotic motion are smaller than those during periodic motion lies in the fact that the periodic motion of the slipper stems from the self-excited vibration of the supersonic slipper-track system, and its energy dissipation rate is not as rapid as that of the slipper in chaotic motion. Therefore, while maintaining strength, designing the slipper to be as short as possible can utilize chaos to reduce the normal contact forces on the slipper.

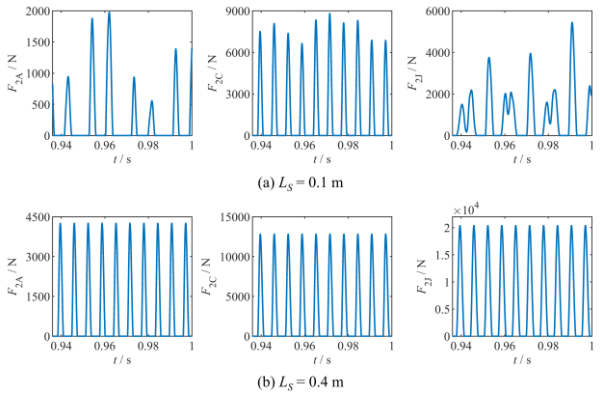

Fig. 12 Normal contact forces at various lengths of slipper: (a) L_S = 0.1 m; (b) L_S = 0.4 m

3.4 Dual-frequency track irregularities

In the above study, the simplification of track irregularities into a single-frequency function aimed to facilitate an intuitive analysis of the impact of a specific frequency on the slipper-track system. However, real track irregularities typically comprise multiple frequency components. In this section, building upon the prior research, track irregularities are modeled as a dual-frequency function to investigate the dynamic responses of this nonlinear system under dual-frequency excitations. Assume that the track irregularities possess two distinct wavelengths, L_{X1} and L_{X2}. Consequently, at the slipper's traveling velocity V_X, the frequencies of track irregularities can be expressed as

$$f_{\mathrm{T}i} = V_X / L_{\mathrm{X}i} \quad (i = 1, 2) . \tag{24}$$

Irregularities of track node $O_{1\mathrm{T}}$ in three directions with respect to time t can be expressed as

$$\begin{cases} P_Y^{1\mathrm{T}} = \mathrm{Amp} \cdot \sum_{i=1}^{2} \sin(2\pi f_{\mathrm{T}i} t) \\ P_Z^{1\mathrm{T}} = \mathrm{Amp} \cdot \sum_{i=1}^{2} \sin(2\pi f_{\mathrm{T}i} t) \\ E_X^{1\mathrm{T}} = \mathrm{Amp}_R \cdot \sum_{i=1}^{2} \sin(2\pi f_{\mathrm{T}i} t) \end{cases} . \tag{25}$$

In addition, track irregularities of track node $O_{2\mathrm{T}}$ can be expressed as

$$\begin{cases} P_Y^{2\mathrm{T}} = \mathrm{Amp} \cdot \sum_{i=1}^{2} \sin[2\pi f_{\mathrm{T}i} (t - L_{\mathrm{S}} / V_X)] \\ P_Z^{2\mathrm{T}} = \mathrm{Amp} \cdot \sum_{i=1}^{2} \sin[2\pi f_{\mathrm{T}i} (t - L_{\mathrm{S}} / V_X)] \\ E_X^{2\mathrm{T}} = \mathrm{Amp}_R \cdot \sum_{i=1}^{2} \sin[2\pi f_{\mathrm{T}i} (t - L_{\mathrm{S}} / V_X)] \end{cases} . \tag{26}$$

In Eqs. (25) and (26), it is observed that the two frequencies $f_{\mathrm{T}1}$ and $f_{\mathrm{T}2}$ of the track irregularities share the amplitude, Amp, and the rotational amplitude, Amp_R. It is worth noting that modeling the two (rotational) amplitudes as equivalent is primarily for mathematical simplification purposes, since real track irregularities may exhibit varying (rotational) amplitudes across different frequencies.

Except for track irregularities, the modeling methods remain consistent with those outlined in Section 2. All simulation parameters are provided in Table 3, and parameters not listed here are identical to those in Table 2. According to Eq. (24), the frequencies of track irregularities are denoted as $f_{\mathrm{T}1}$ = 150 Hz and $f_{\mathrm{T}2}$ = 125 Hz, respectively. Following simulation, the PSD of vertical acceleration A_Z, roll angular acceleration α_X, and pitch angular acceleration α_Y of the slipper are presented in Fig. 13, with a frequency analysis range spanning from 0 to 520 Hz. Due to the introduction of two frequencies in the track irregularities, the inherent dynamic characteristics of the supersonic slipper-track system undergo alterations. Figure 13 clearly illustrates that the energy of each dynamic response of the slipper predominantly concentrates at discrete frequencies, resulting in multiple spikes within the curves. This study identifies the frequencies corresponding to relatively prominent spikes in Fig. 13. In the spectrum of the three responses, all of them exhibit harmonic components at frequencies $f_{\mathrm{T}1}$ and $f_{\mathrm{T}2}$, with the highest spikes aligning with the frequency $f_{\mathrm{T}1}$ of the track irregularity. This signifies that within each response, the frequency of the harmonic component

with the greatest amplitude is f_{T1}. The frequency spectrum of pitch angular acceleration α_Y reveals the presence of harmonic frequencies that include integer multiples of frequencies f_{T1} or f_{T2}, such as $2f_{T1}$, $3f_{T2}$, and $4f_{T2}$. These high-order harmonics arise due to nonlinear factors within the system, including clearances and contacts. Moreover, among the harmonic frequencies within the three dynamic responses, there exist combined frequencies involving mf_{T1} and nf_{T2} (where m and n are integers), such as $2f_{T2} - f_{T1}$, $2f_{T1} - f_{T2}$, $f_{T1} + f_{T2}$, $3f_{T1} - f_{T2}$, $4f_{T2} - f_{T1}$, $f_{T1} + 2f_{T2}$, $2f_{T1} + f_{T2}$, and $4f_{T1} - f_{T2}$. This phenomenon of frequency coupling, fundamentally deviating from the superposition principle of linear systems, represents another crucial characteristic of nonlinear systems. The aforementioned harmonic components, corresponding to the frequencies of the track irregularities, their integer multiples, and the combined frequencies, collectively contribute to the formation of the nonlinear dynamic responses exhibited by the supersonic slipper-track system. Considering the above analysis, it is advisable to minimize the presence of periodic track irregularities during track installation, as the frequency corresponding to this periodicity will inevitably manifest in the dynamic responses of the slipper. Additionally, if the frequencies linked to high-amplitude harmonic components in the track irregularities have been measured and determined, it is prudent to design the rocket sled in a manner that ensures its natural frequencies are sufficiently distant from these frequencies. Simultaneously, efforts should be made to prevent the natural frequencies of the rocket sled from coinciding with integer multiples or nonlinear combinations of these frequencies.

Table 3 Parameters for analysis of dual-frequency track irregularities

Parameter	Value
Traveling velocity of slipper V_X	1500 m s^{-1}
Slipper-track clearance value C	1 mm
Length of slipper L_S	0.2 m
Wavelength of track irregularity L_{X1}	10 m
Wavelength of track irregularity L_{X2}	12 m
Integral step	10^{-6} s

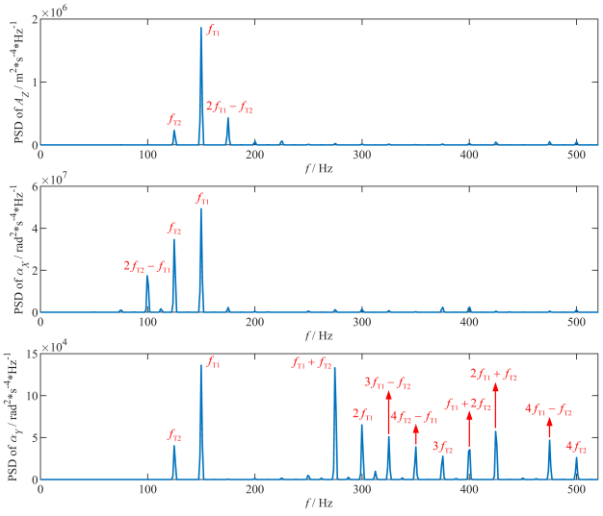

Fig. 13 PSD of slipper accelerations

4 Conclusions

The dynamic model of the supersonic slipper-track system was developed, considering essential factors such as slipper-track clearance, track irregularities, and the influence of normal contact forces. To comprehensively understand the system's dynamic responses, an examination was conducted from both time and frequency domain perspectives. This investigation led to the discovery of notable phenomena, including self-excited vibrations and super-harmonic responses within the supersonic slipper-track system. Furthermore, when the track irregularities were approximated as a dual-frequency function, the responses revealed harmonic components corresponding to nonlinear combined frequencies.

The bifurcation analysis encompassed a wide range of parameters, including slipper's traveling velocity, slipper-track clearance value, and slipper length. Notably, the bifurcation points of the system under various parameter settings were identified. Among these findings, the presence of jumping phenomena in the bifurcation diagrams concerning slipper's traveling velocity was intriguing. From both a vibration reduction and predictability perspective, the evidence pointed towards the benefits of designing smaller slipper-track clearances. In the analysis focused on the length of the slipper, an intriguing revelation emerged, suggesting that chaos could be harnessed effectively to reduce the normal contact forces exerted on the slipper.

For chaos identification, a multifaceted approach was adopted, including qualitative and quantitative assessments employing phase diagrams, Poincaré sections, tracking the trajectory of the slipper's center, and calculating the largest Lyapunov exponent. The combination of these various parameters yielded a diverse

array of nonlinear behaviors for the slipper, including period-1, period-2, period-3, quasiperiodic, and chaotic motions. The type of attractor transitioned between fixed points, limit cycles, and strange attractors, underscoring the complexity of the system's behavior.

In summary, this study provided insights into the prediction of nonlinear behaviors within the slipper-track system. Additionally, it contributed to enhancing our understanding of control parameter rationalization and optimizing the design of both the slipper and the track. Moreover, this research serves as a foundational reference for future bifurcation analysis and chaos identification within the broader context of supersonic rocket sled and track systems.

Acknowledgment

The first author gratefully acknowledges the China Scholarship Council (CSC) (grant number 202106280004). The fourth author gratefully acknowledges the China Scholarship Council (CSC) (grant number 202206280003).

Funding Data

China Scholarship Council (CSC) (grant numbers 202106280004, 202206280003).

Data Availability Statement

The datasets generated and supporting the findings of this article are obtainable from the corresponding author upon reasonable request.

Competing Interests

The last author, Pierangelo Masarati, is an Associate Editor of ASME Journal of Computational and Nonlinear Dynamics. The authors have no relevant financial or non-financial interests to disclose.

Appendix

A.1 Detailed dynamic equations of the supersonic slipper-track system.

In the first row of Eq. (13), the generalized mass matrix **M** can be expressed as

$$\mathbf{M} = diag\left\{M, M, M, J_X, J_Y, J_Z, \mathbf{0}_{1\times6}, \mathbf{0}_{1\times6}\right\} \tag{A1}$$

where the first six terms represent the mass and inertia of the slipper node, and the last two terms correspond to two track nodes. ~~Since positions and orientations of the two track nodes with respect to time are determined, there is no need to give them mass and inertia.~~ The vector of generalized coordinates $\mathbf{x}$ can be expressed as

$$\begin{aligned}\mathbf{x} = [&P_X^{\mathrm{S}}(t), P_Y^{\mathrm{S}}(t), P_Z^{\mathrm{S}}(t), E_X^{\mathrm{S}}(t), E_Y^{\mathrm{S}}(t), E_Z^{\mathrm{S}}(t),\\ &P_X^{1\mathrm{T}}(t), P_Y^{1\mathrm{T}}(t), P_Z^{1\mathrm{T}}(t), E_X^{1\mathrm{T}}(t), E_Y^{1\mathrm{T}}(t), E_Z^{1\mathrm{T}}(t),\\ &P_X^{2\mathrm{T}}(t), P_Y^{2\mathrm{T}}(t), P_Z^{2\mathrm{T}}(t), E_X^{2\mathrm{T}}(t), E_Y^{2\mathrm{T}}(t), E_Z^{2\mathrm{T}}(t)]^{\mathrm{T}}\end{aligned} \tag{A2}$$

where P_i^j and E_i^j are the position and Euler angle of node j (j = S, 1T, 2T) in the i direction (i = X, Y, Z). The vector of generalized momentum $\boldsymbol{\beta}$ can be expressed as

$$\boldsymbol{\beta} = \begin{bmatrix}\boldsymbol{\beta}_{\mathrm{S}}(t)\\ \boldsymbol{\gamma}_{\mathrm{S}}(t)\\ \mathbf{0}_{12\times1}\end{bmatrix} \tag{A3}$$

where $\boldsymbol{\beta}_{\mathrm{S}}$ and $\boldsymbol{\gamma}_{\mathrm{S}}$ are the momentum and momenta moment vectors of the slipper node in three directions, respectively. Since the two track nodes do not have mass and inertia, their momentum and momenta moment are considered meaningless. The detailed formulation of the second row of Eq. (13) can be expressed as

$$\begin{aligned}\dot{\boldsymbol{\beta}}_{\mathrm{S}}(t) = &\mathbf{F}_{1\mathrm{A}}(t) + \mathbf{F}_{1\mathrm{B}}(t) + \mathbf{F}_{1\mathrm{C}}(t) + \mathbf{F}_{1\mathrm{D}}(t) + \mathbf{F}_{1\mathrm{E}}(t) + \mathbf{F}_{1\mathrm{F}}(t) + \mathbf{F}_{1\mathrm{G}}(t) + \mathbf{F}_{1\mathrm{H}}(t) + \mathbf{F}_{1\mathrm{I}}(t) + \mathbf{F}_{1\mathrm{J}}(t) +\\ &\mathbf{F}_{2\mathrm{A}}(t) + \mathbf{F}_{2\mathrm{B}}(t) + \mathbf{F}_{2\mathrm{C}}(t) + \mathbf{F}_{2\mathrm{D}}(t) + \mathbf{F}_{2\mathrm{E}}(t) + \mathbf{F}_{2\mathrm{F}}(t) + \mathbf{F}_{2\mathrm{G}}(t) + \mathbf{F}_{2\mathrm{H}}(t) + \mathbf{F}_{2\mathrm{I}}(t) + \mathbf{F}_{2\mathrm{J}}(t)\end{aligned} \tag{A4a}$$

$$\begin{aligned}\dot{\boldsymbol{\gamma}}_{\mathrm{S}}(t) = &\mathbf{w}_{1\mathrm{S}}^{A}(t)\times\mathbf{F}_{1\mathrm{A}}(t) + \mathbf{w}_{1\mathrm{S}}^{B}(t)\times\mathbf{F}_{1\mathrm{B}}(t) + \mathbf{w}_{1\mathrm{S}}^{C}(t)\times\mathbf{F}_{1\mathrm{C}}(t) + \mathbf{w}_{1\mathrm{S}}^{D}(t)\times\mathbf{F}_{1\mathrm{D}}(t) +\\ &\mathbf{w}_{1\mathrm{S}}^{E}(t)\times\mathbf{F}_{1\mathrm{E}}(t) + \mathbf{w}_{1\mathrm{S}}^{F}(t)\times\mathbf{F}_{1\mathrm{F}}(t) + \mathbf{w}_{1\mathrm{S}}^{G}(t)\times\mathbf{F}_{1\mathrm{G}}(t) + \mathbf{w}_{1\mathrm{S}}^{H}(t)\times\mathbf{F}_{1\mathrm{H}}(t) +\\ &\mathbf{w}_{1\mathrm{S}}^{I}(t)\times\mathbf{F}_{1\mathrm{I}}(t) + \mathbf{w}_{1\mathrm{S}}^{J}(t)\times\mathbf{F}_{1\mathrm{J}}(t) + \mathbf{w}_{2\mathrm{S}}^{A}(t)\times\mathbf{F}_{2\mathrm{A}}(t) + \mathbf{w}_{2\mathrm{S}}^{B}(t)\times\mathbf{F}_{2\mathrm{B}}(t) +\\ &\mathbf{w}_{2\mathrm{S}}^{C}(t)\times\mathbf{F}_{2\mathrm{C}}(t) + \mathbf{w}_{2\mathrm{S}}^{D}(t)\times\mathbf{F}_{2\mathrm{D}}(t) + \mathbf{w}_{2\mathrm{S}}^{E}(t)\times\mathbf{F}_{2\mathrm{E}}(t) + \mathbf{w}_{2\mathrm{S}}^{F}(t)\times\mathbf{F}_{2\mathrm{F}}(t) +\\ &\mathbf{w}_{2\mathrm{S}}^{G}(t)\times\mathbf{F}_{2\mathrm{G}}(t) + \mathbf{w}_{2\mathrm{S}}^{H}(t)\times\mathbf{F}_{2\mathrm{H}}(t) + \mathbf{w}_{2\mathrm{S}}^{I}(t)\times\mathbf{F}_{2\mathrm{I}}(t) + \mathbf{w}_{2\mathrm{S}}^{J}(t)\times\mathbf{F}_{2\mathrm{J}}(t) -\\ &\dot{\mathbf{r}}_{\mathrm{S}}(t)\times\boldsymbol{\beta}_{\mathrm{S}}(t)\end{aligned} \tag{A4b}$$

where $\mathbf{F}_{ij}$ is the normal contact force vector at point $j_{i\mathrm{S}}$, which is computed through Eq. (12) and relevant to $\mathbf{x}$ and $\dot{\mathbf{x}}$, and $\mathbf{w}_{i\mathrm{S}}^{j}$ is the position vector from the slipper node O_{S} to point $j_{i\mathrm{S}}$ (i = 1 or 2, j = A ~ J).

The detailed formulation of the third row of Eq. (13) can be expressed as

$$\begin{cases} P_X^{1\mathrm{T}}(t) - P_X^{\mathrm{S}}(t) - L_{\mathrm{S}}/2 = 0 \\ P_Y^{1\mathrm{T}}(t) - \mathrm{Amp}\cdot\sin(2\pi f_{\mathrm{T}} t) = 0 \\ P_Z^{1\mathrm{T}}(t) - \mathrm{Amp}\cdot\sin(2\pi f_{\mathrm{T}} t) = 0 \\ E_X^{1\mathrm{T}}(t) - \mathrm{Amp}_R\cdot\sin(2\pi f_{\mathrm{T}} t) = 0 \\ E_Y^{1\mathrm{T}}(t) = 0 \\ E_Z^{1\mathrm{T}}(t) = 0 \\ P_X^{2\mathrm{T}}(t) - P_X^{\mathrm{S}}(t) + L_{\mathrm{S}}/2 = 0 \\ P_Y^{2\mathrm{T}}(t) - \mathrm{Amp}\cdot\sin[2\pi f_{\mathrm{T}}(t - L_{\mathrm{S}}/V_X)] = 0 \\ P_Z^{2\mathrm{T}}(t) - \mathrm{Amp}\cdot\sin[2\pi f_{\mathrm{T}}(t - L_{\mathrm{S}}/V_X)] = 0 \\ E_X^{2\mathrm{T}}(t) - \mathrm{Amp}_R\cdot\sin[2\pi f_{\mathrm{T}}(t - L_{\mathrm{S}}/V_X)] = 0 \\ E_Y^{2\mathrm{T}}(t) = 0 \\ E_Z^{2\mathrm{T}}(t) = 0 \end{cases} \tag{A5}$$

The detailed formulation of the last row of Eq. (13) can be expressed as

$$\dot{P}_X^{\mathrm{S}}(t) - V_X \equiv 0 \tag{A6}$$

References

[1] Dang, T., Li, B., Hu, D., Sun, Y., and Liu, Z., 2021, "Aerodynamic design optimization of a hypersonic rocket sled deflector using the free-form deformation technique," Proc. Inst. Mech. Eng. Part G-J. Aerosp. Eng., **235**(15), pp. 2240-2248. https://doi.org/10.1177/0954410021994984.

[2] Walia, S., Satya, V., Malik, S., Chander, S., Devi, S., and Sharma, A.C., 2022, "Rocket Sled Based High Speed Rail Track Test Facilities: A Review," Def. Sci. J., **72**(2), pp. 182-194. https://doi.org/10.14429/dsj.72.17014.

[3] Salahshoor, E., Ebrahimi, S., and Zhang, Y., 2018, "Frequency analysis of a typical planar flexible multibody system with joint clearances," Mech. Mach. Theory, **126**, pp. 429-456. https://doi.org/10.1016/j.mechmachtheory.2018.04.027.

[4] Xiao, M., Geng, G., Li, G., Li, H., and Ma, R., 2017, "Analysis on dynamic precision reliability of high-speed precision press based on Monte Carlo method," Nonlinear Dyn., **90**, pp. 2979-2988. https://doi.org/10.1007/s11071-017-3857-7.

[5] Tian, Q., Flores, P., and Lankarani, H.M., 2018, "A comprehensive survey of the analytical, numerical and experimental methodologies for dynamics of multibody mechanical systems with clearance or

638 imperfect joints," Mech. Mach. Theory, **122**, pp. 1-57.
639 https://doi.org/10.1016/j.mechmachtheory.2017.12.002.
640 [6] Amiri, A., Dardel, M., and Daniali, H.M., 2019, "Effects of passive vibration absorbers on the
641 mechanisms having clearance joints," Multibody Syst. Dyn., **47**, pp. 363-395.
642 https://doi.org/10.1007/s11044-019-09684-2.
643 [7] Wu, L., Marghitu, D.B., and Zhao, J., 2017, "Nonlinear dynamics response of a planar mechanism with
644 two driving links and prismatic pair clearance," Math. Probl. Eng. 2017, pp. 1-12.
645 https://doi.org/10.1155/2017/4295805.
646 [8] Song, N., Peng, H., and Kan, Z., 2022, "Nonsmooth strategy for rigid-flexible multibody system
647 considering different types of clearance joints and lubrication," Multibody Syst. Dyn., **55**(3), pp. 341-374.
648 https://doi.org/10.1007/s11044-022-09827-y.
649 [9] Xiao, S., Liu, S., Wang, H., Lin, Y., Song, M., and Zhang, H., 2020, "Nonlinear dynamics of coupling
650 rub-impact of double translational joints with subsidence considering the flexibility of piston rod,"
651 Nonlinear Dyn., **100**, pp. 1203-1229. https://doi.org/10.1007/s11071-020-05566-x.
652 [10] Stoenescu, E.D., and Marghitu, D.B., 2003, "Dynamic analysis of a planar rigid-link mechanism with
653 rotating slider joint and clearance," J. Sound Vib., **266**(2), pp. 394-404. https://doi.org/10.1016/S0022-
654 460X(03)00053-1.
655 [11] Flores, P., Ambrósio, J., Claro, J.C.P., and Lankarani, H.M., 2008, "Translational joints with clearance
656 in rigid multibody systems," J. Comput. Nonlinear Dyn., **3**(011007), pp. 1-10.
657 https://doi.org/10.1115/1.2802113.
658 [12] Flores, P., Leine, R., and Glocker, C., 2010, "Modeling and analysis of rigid multibody systems with
659 translational clearance joints based on the nonsmooth dynamics approach," Multibody Syst. Dyn., **23**, pp.
660 165-190. https://doi.org/10.1007/s11044-009-9178-y.
661 [13] Chen, X., Jiang, S., and Deng, Y., 2020, "Dynamic responses of planar multilink mechanism
662 considering mixed clearances," Shock Vib., **2020**, pp. 1-18. https://doi.org/10.1155/2020/8725845.
663 [14] Wu, X., Sun, Y., Wang, Y., and Chen, Y., 2021, "Correlation dimension and bifurcation analysis for
664 the planar slider-crank mechanism with multiple clearance joints," Multibody Syst. Dyn., **52**, pp. 95-116.
665 https://doi.org/10.1007/s11044-020-09769-3.

[15] Xiao, L., Yan, F., Chen, T., Zhang, S., and Jiang, S., 2023, "Study on nonlinear dynamics of rigid-flexible coupling multi-link mechanism considering various kinds of clearances," Nonlinear Dyn., **111**(4), pp. 3279-3306. https://doi.org/10.1007/s11071-022-08033-x.

[16] Zhuang, F., and Wang, Q., 2013, "Modeling and simulation of the nonsmooth planar rigid multibody systems with frictional translational joints," Multibody Syst. Dyn., **29**, pp. 403-423. https://doi.org/10.1007/s11044-012-9328-5.

[17] Zhang, J., and Wang, Q., 2016, "Modeling and simulation of a frictional translational joint with a flexible slider and clearance," Multibody Syst. Dyn., **38**, pp. 367-389. https://doi.org/10.1007/s11044-015-9474-7.

[18] Zheng, X., Li, J., Wang, Q., and Liao, Q., 2019, "A methodology for modeling and simulating frictional translational clearance joint in multibody systems including a flexible slider part," Mech. Mach. Theory, **142**(103603), pp. 1-14. https://doi.org/10.1016/j.mechmachtheory.2019.103603.

[19] Wu, X., Sun, Y., Wang, Y., and Chen, Y., 2020, "Dynamic analysis of the double crank mechanism with a 3D translational clearance joint employing a variable stiffness contact force model," Nonlinear Dyn., **99**, pp. 1937-1958. https://doi.org/10.1007/s11071-019-05419-2.

[20] Qian, M., Qin, Z., Yan, S., and Zhang, L., 2020, "A comprehensive method for the contact detection of a translational clearance joint and dynamic response after its application in a crank-slider mechanism," Mech. Mach. Theory, **145**(103717), pp. 1-19. https://doi.org/10.1016/j.mechmachtheory.2019.103717.

[21] Qi, Z., Luo, X., and Huang, Z., 2011, "Frictional contact analysis of spatial prismatic joints in multibody systems," Multibody Syst. Dyn., **26**, pp. 441-468. https://doi.org/10.1007/s11044-011-9264-9.

[22] Xu, M., Li, C., Sun, Y., Yang, T., Zhang, H., Liu, Z., Liu, H., Li, Z., and Zhang, Y., 2021, "Model and nonlinear dynamic analysis of linear guideway subjected to external periodic excitation in five directions," Nonlinear Dyn., **105**(4), pp. 3061-3092. https://doi.org/10.1007/s11071-021-06796-3.

[23] Liu, Z., Xu, M., Zhang, H., Li, C., Yao, G., Li, Z., Miao, H., Wang, C., and Zhang, Y., 2022, "Modeling and analyzing of nonlinear dynamics for linear guide slide platform considering assembly error," Nonlinear Dyn., **108**(3), pp. 2193-2221. https://doi.org/10.1007/s11071-022-07345-2.

[24] Xu, M., Li, C., Zhang, H., Liu, Z., and Zhang, Y., 2021, "A comprehensive nonlinear dynamic model for ball screw feed system with rolling joint characteristics," Nonlinear Dyn., **106**(1), pp. 169-210. https://doi.org/10.1007/s11071-021-06815-3.

[25] Zeng, X.H., Shi, H.M., and Wu, H., 2021, "Nonlinear dynamic responses of high-speed railway vehicles under combined self-excitation and forced excitation considering the influence of unsteady aerodynamic loads," Nonlinear Dyn., **105**, pp. 3025-3060. https://doi.org/10.1007/s11071-021-06795-4.

[26] Wang, X., Lu, Z., Wen, J., Wei, J., and Wang, Z., 2022, "Kinematics modelling and numerical investigation on the hunting oscillation of wheel–rail nonlinear geometric contact system," Nonlinear Dyn., **107**(3), pp. 2075-2097. https://doi.org/10.1007/s11071-021-07103-w.

[27] Guo, J., Shi, H., Luo, R., and Zeng, J., 2021, "Bifurcation analysis of a railway wheelset with nonlinear wheel–rail contact," Nonlinear Dyn., **104**(2), pp. 989-1005. https://doi.org/10.1007/s11071-021-06373-8.

[28] Zboinski, K., and Dusza, M., 2017, "Bifurcation analysis of 4-axle rail vehicle models in a curved track," Nonlinear Dyn., **89**(2), pp. 863-885. https://doi.org/10.1007/s11071-017-3489-y.

[29] Xiao, J., Zhang, W.W., Xue, Q., Gao, W.B., and Zhang, L.R., 2019, "Analysis of boot rail collision resistance in rocket sled test system," IOP Conf. Ser.: Mater. Sci. Eng., **657**(012028), pp. 1-7. https://doi.org/10.1088/1757-899X/657/1/012028.

[30] Turnbull, D., Hooser, C., Hooser, M., and Myers, J., 2010, "Soft sled test capability at the Holloman High Speed Test Track," U.S. Air Force T&E Days, Nashville, Tennessee, February 2-4, 2010, pp. 1-12. https://doi.org/10.2514/6.2010-1708.

[31] Dang, T., Liu, Z., Zhou, X., Sun, Y., and Zhao, P., 2022, "Dynamic Response of a Hypersonic Rocket Sled Considering Friction and Wear," J. Spacecr. Rocket., **59**(4), pp. 1289-1303. https://doi.org/10.2514/1.A35267.

[32] Dang, T., Morandini, M., Masarati, P., Liu, Z., and Zhou, J., 2023, "Efficient computational method for multibody dynamics of supersonic intermittent contact system," 11th ECCOMAS Themat. Conf. Multibody Dyn., Lisbon, Portugal, July 24-28, 2023, pp. 1-7. https://re.public.polimi.it/bitstream/11311/1247480/1/DANGT01-23.pdf.

[33] Hooser, M., 2018, "Soft sled-the low vibration sled test capability at the Holloman High Speed Test Track," Aerodyn. Meas. Technol. Ground Test. Conf., Atlanta, Georgia, June 25-29, 2018, pp. 1-10. https://doi.org/10.2514/6.2018-3872.

[34] Liu, J., Zhao, H., Gu, K., and Wang, W., 2017, "An analysis of dynamic response of a rocket sled," 2017 2nd Int. Conf. Artif. Intell. Eng. Appl., pp. 956-967.

https://scholar.archive.org/work/p4slcw4ds5db5kafqihx2s7fou/access/wayback/http://dpi-proceedings.com/index.php/dtcse/article/download/15034/14547.

[35] Zhang, J.H., and Jiang, S.S., 2012, "Rigid-Flexible coupling model and dynamic analysis of rocket sled," Adv. Mater. Res., **346**, pp. 447-454. https://doi.org/10.4028/www.scientific.net/AMR.346.447.

[36] Li, H., Yan, H., Hu, B., and Yang, M., 2020, "Research on calibration method and effect evaluation of rocket sled track profile irregularity," 7th Int. Forum Electr. Eng. Autom., Hefei, China, September 25-27, 2020, pp. 203-206. https://doi.org/10.1109/IFEEA51475.2020.00049.

[37] Chen, S.Y., He, Y.L., and Li, Z.W., 2014, "Analysis of the rocket sled track irregularity in time and frequency domains," CICTP 2014: Safe Smart Sustain. Multimodal Transp. Syst., pp. 111-118. https://doi.org/10.1061/9780784413623.012.

[38] Yadav, A., Jain, A., and Chander, S., 2021, "Modelling and analysis of pivoted slipper and its component at 40 ton load," Adv. Eng. Des.-Sel. Proc. ICOIED 2020, pp. 373-383. https://doi.org/10.1007/978-981-33-4018-3_35.

[39] Gerasimov, S.I., Erofeev, V.I., Kamchatnyi, V.G., and Odzerikho, I.A., 2018, "The sliding contact condition in stability analysis of stage motion for a rocket sled track facility," J. Mach. Manuf. Reliab., **47**, pp. 221-226. https://doi.org/10.3103/S105261881803007X.

[40] Corral, E., Moreno, R.G., García, M.G., and Castejón, C., 2021, "Nonlinear phenomena of contact in multibody systems dynamics: a review," Nonlinear Dyn., **104**, pp. 1269-1295. https://doi.org/10.1007/s11071-021-06344-z.

[41] Magalhães, H., Marques, F., Liu, B., Antunes, P., Pombo, J., Flores, P., Ambrósio, J., Piotrowski, J., and Bruni, S., 2020, "Implementation of a non-Hertzian contact model for railway dynamic application," Multibody Syst. Dyn., **48**, pp. 41-78. https://doi.org/10.1007/s11044-019-09688-y.

[42] Askari, E., Flores, P., Dabirrahmani, D., and Appleyard, R., 2014, "Nonlinear vibration and dynamics of ceramic on ceramic artificial hip joints: a spatial multibody modelling," Nonlinear Dyn., **76**, pp. 1365-1377. https://doi.org/10.1007/s11071-0131215-y.

[43] Flores, P., Machado, M., Silva, M.T., and Martins, J.M., 2011, "On the continuous contact force models for soft materials in multibody dynamics," Multibody Syst. Dyn., **25**(3), pp. 357-375. https://doi.org/10.1007/s11044-010-9237-4.

752 [44] Hunt, K.H., and Crossley, F.R.E., 1975, "Coefficient of restitution interpreted as damping in
753 vibroimpact," ASME. J. Appl. Mech., **42**(2), pp. 440-445. https://doi.org/10.1115/1.3423596.
754 [45] Lankarani, H.M., and Nikravesh, P.E., 1994, "Continuous contact force models for impact analysis in
755 multibody systems," Nonlinear Dyn., **5**(2), pp.193-207. https://doi.org/10.1007/BF00045676.
756 [46] Masarati, P., Morandini, M., and Mantegazza, P., 2014, "An efficient formulation for general-purpose
757 multibody/multiphysics analysis," J. Comput. Nonlinear Dyn., **9**(041001), pp. 1-9.
758 https://doi.org/10.1115/1.4025628.
759 [47] Zhang, H., Zhang, R., Zanoni, A., and Masarati, P., 2022, "Performance of implicit A-stable time
760 integration methods for multibody system dynamics," Multibody Syst. Dyn., **54**(3), pp. 263-301.
761 https://doi.org/10.1007/s11044-021-09806-9.
762 [48] Lyapunov, A.M., 1992, "The general problem of the stability of motion," Int. J. Control, **55**(3), pp.
763 531-534. https://doi.org/10.1080/00207179208934253.
764
765

766

Figure Captions List

Fig. 1 Schematic diagram of rocket sled system

Fig. 2 Several models of systems traveling along guide rails: (a) planar translational clearance joint; (b) spatial translational clearance joint; (c) slipper-track system; (d) linear guide slide platform; (e) vehicle wheel-rail system

Fig. 3 Analysis model for slipper-track system: (a) xz-plane; (b) yz-plane

Fig. 4 Dynamic responses of slipper at various traveling velocities: (a) V_X = 900 m s^{-1}; (b) V_X = 1500 m s^{-1}; (c) V_X = 2300 m s^{-1}

Fig. 5 Bifurcation diagrams concerning traveling velocity of slipper

Fig. 6 LLE vs. traveling velocity of slipper

Fig. 7 Dynamic responses of slipper at various clearance values: (a) C = 1 mm; (b) C = 4 mm

Fig. 8 Bifurcation diagrams concerning slipper-track clearance value

Fig. 9 LLE vs. slipper-track clearance value

Fig. 10 Bifurcation diagrams concerning length of slipper

Fig. 11 LLE vs. length of slipper

Fig. 12 Normal contact forces at various lengths of slipper: (a) L_S = 0.1 m; (b) L_S = 0.4 m

Fig. 13 PSD of slipper accelerations

767

Table Caption List

Table 1 Relative positions of each contact point and slipper node

Table 2 Parameters for dynamic model

Table 3 Parameters for analysis of dual-frequency track irregularities

768
769